

ThermoPore: Predicting Part Porosity Based on Thermal Images Using Deep Learning

Peter Myung-Won Pak,^{*,†} Francis Ogoke,^{*,†} Andrew Polonsky,^{*,‡} Anthony Garland,^{*,‡} Dan S. Bolintineanu,^{*,‡} Dan R. Moser,^{*,‡} Michael J. Heiden,^{*,‡} and Amir Barati Farimani^{*,†,¶}

[†] *Department of Mechanical Engineering, Carnegie Mellon University, Pittsburgh, PA, USA*

[‡] *Sandia National Laboratories*

[¶] *Machine Learning Department, Carnegie Mellon University, Pittsburgh, PA, USA*

E-mail: ppak@cmu.edu; oogoke@andrew.cmu.edu; apolon@sandia.gov; agarlan@sandia.gov; dsbolin@sandia.gov; dmoser@sandia.gov; mheiden@sandia.gov; barati@cmu.edu

Abstract

We present a deep learning approach for quantifying and localizing *ex-situ* porosity within Laser Powder Bed Fusion fabricated samples utilizing *in-situ* thermal image monitoring data. Our goal is to build the real time porosity map of parts based on thermal images acquired during the build. The quantification task builds upon the established Convolutional Neural Network model architecture to predict pore count and the localization task leverages the spatial and temporal attention mechanisms of the novel Video Vision Transformer model to indicate areas of expected porosity. Our model for porosity quantification achieved a R^2 score of 0.57 and our model for porosity localization produced an average IoU score of 0.32 and a maximum of 1.0. This work is setting the foundations of part porosity "Digital Twins" based on additive manufacturing monitoring data and can be applied downstream to reduce time-intensive

post-inspection and testing activities during part qualification and certification. In addition, we seek to accelerate the acquisition of crucial insights normally only available through *ex-situ* part evaluation by means of machine learning analysis of *in-situ* process monitoring data.

Introduction

Additive manufacturing (AM) presents a competitive alternative to the conventional approaches in manufacturing with the advantages of efficient material utilization, design consolidation, and fast iteration.¹⁻⁴ However, a significant area of improvement lies within defect prevention as printed parts present their own set of challenges in porosity, distortion, and cracking.¹ These issues are often uncovered through *ex-situ* non-destructive testing methods and can sometimes be addressed through lengthy post-processing means such as hot isostatic pressing (HIPing) before they are certified.^{5,6} With *in-situ* process monitoring, a digital twin of the fabrication process can be created and segments of the certification process can be conducted in parallel.⁷⁻⁹

Laser powder bed fusion (LPBF), relies primarily on established process maps¹⁰⁻¹² to determine the optimal machine settings that minimize defects within the finished part. Most commonly, these process maps explore the power and velocity space to determine a combination of two that would result in a sufficiently dense part. Informed control over these process parameters and others such as hatch spacing,¹³ layer height,¹⁴ and raster pattern,¹⁵ can greatly affect the part's porosity, microstructure,¹⁶ and surface finish.¹⁴ However, even within build conditions with nominal process parameters, defects such as porosity remain an issue.¹⁷

In-situ process monitoring offers a means to resolve this issue as information obtained from the build process can assist in resolving many of the technical challenges encountered during part fabrication.¹⁷⁻¹⁹ Many of these defects and their precursors such as part distortions,²⁰ surface roughness,²¹ or keyhole formation^{22,23} exhibit signals which with the

appropriate sensors can be detected before *ex-situ* sample analysis. These indicators can be applied alongside the build process to analytical and machine learning models in order to obtain the necessary feedback to adjust process parameters for the build. This feedback loop would be optimized to reduce the number of part defects through both preemptive and responsive measures.^{24,25} In addition, reconstructing the porosity map can significantly accelerate the part certification process as the knowledge of the porosity map can expedite qualification through observations of statistics alone.^{7,26-29}

Thermal imaging demonstrates effectiveness as an *in-situ* process monitoring technique as evidenced by previous studies which have explored comparing melt pool images to computational fluid dynamics simulations,³⁰ mathematical equations,³¹ and 3D surface maps.³² Further exploration of this technique has shown effectiveness in applications such as defect detection and correction within the build process either indicating likely porosity given a thermal image of a melt pool³³ or material extrusion correction in large scale additive manufacturing.^{34,35}

Analytical solutions such as Rosenthal's equation³⁶ provide a foundational method to determine nominal process parameter regions within laser power and scanning velocity space. This equation can be adapted to provide depth and width estimates of the melt pool given specific process parameters such as preheat temperature, power, and velocity which can be applied to the selection of nominal parameters for hatch spacing and layer height. However, this method poses limitations as solutions provided by Rosenthal's equation are only suitable for melt pools within the conduction regime.³⁶⁻³⁸ This leaves areas out that are not captured through analytical models such as melt pool behavior in the keyhole mode and process conditions such as scan strategies.

Much attention has been directed towards machine learning to fill this gap between the projection of these analytical models and their applied results some of which include process parameter optimizing^{39,40} and fatigue life prediction.⁴¹ In this paper we explore the application of machine learning towards the quantification and spatial localization of pores

within a sample given the *in-situ* monitoring data of thermal images. These predictions can then be utilized to create a digital twin of the built sample and perform qualification and certification tasks in parallel to the sample fabrication.⁷⁻⁹

For the task of pore quantification a three dimensional Convolutional Neural Network (CNN) was utilized to extract features within a provided sequence of thermal images and provide a singular scalar prediction of the expected number of pores. Models such as *ImageNet*⁴² have shown the effectiveness of 2D CNNs with image classification tasks and other models such as *C3D*⁴³ have applied this technique to extended over a sequence of images. Training a 3D CNN model with the objective of pore quantification enables the identification of pore counts within a build layer prior to any *ex-situ* sample analysis.

The task of pore localization utilizes a Video Vision Transformer (ViViT)⁴⁴ which is suited to capture the spatial and temporal features within the sequence of thermal images through subdividing the input into patches. The original implementation of the ViViT model is structured to provide a classification output,⁴⁴ however for the purposes of pore localization the classification head is replaced with a dense prediction head which retains the spatial information of the input sequence. Our network implementation utilizes a dense output which directly correlates the spatial and temporal information into a 2D pore localization prediction. This network builds off the work by Ranftl et al.⁴⁵ where fusion blocks and convolutional layers are added to a vision transformer to provide depth predictions of a given image.

Additive manufacturing, specifically LPBF, relies on sample *ex-situ* post-build inspection and testing to qualify parts and identify potential defects encountered during the build process.^{27,46-48} This often includes tedious processes such as cross-sectional imaging or x-ray computed micro-tomography (CT) after the part fabrication. However, if similar information is obtained earlier during the build process through the creation of a digital twin, builds can be terminated earlier or dynamic adjustments can be applied once the presence of defects is detected to reduce material waste and costs. Applying machine learning techniques such

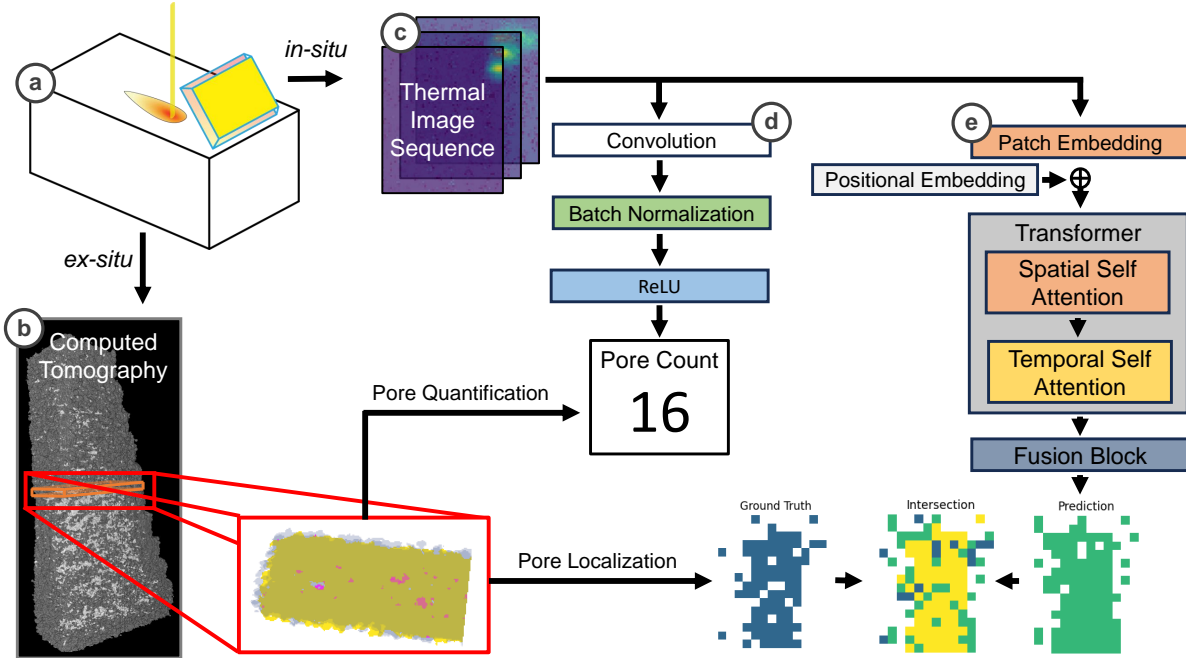


Figure 1: A sequence of 200 thermal pyrometry images (1c) providing absolute temperature values of the build plate taken *in-situ* (1a) are provided as input data for models for pore quantification (1d) and pore localization (1e). These two separate models utilize a CNN and ViViT with dense output heads to produce a scalar number of pores and 2D mapping of expected porosity regions respectively. Metrics derived from *ex-situ* CT data for the corresponding build layer are used as ground truth values for each model (1b).

as CNN or ViViT models on *in-situ* data opens the possibility to acquire *ex-situ* sample insights during the build process and fabricate parts within a closed feedback loop.

Methodology

Spacing and *Velocity* Samples

Sample Fabrication and Data Acquisition

This paper analyzes two samples, one with variable hatch spacing (*Spacing*) and the other with variable scan velocity (*Velocity*). Both of these samples were manufactured using LPBF equipment (ProX DMP 200 from 3D Systems) with AISI 316L stainless steel powder and a constant laser power of 103 W.^{33,49} These samples were designed with a staircase structure

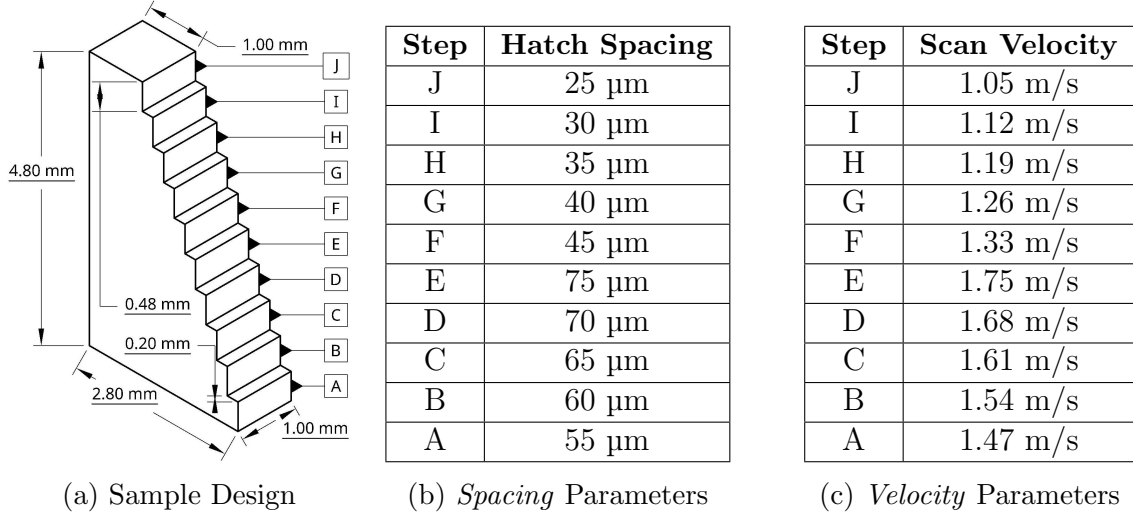


Figure 2: Each sample (2a) contains 10 different process parameter combinations with the *Spacing* sample (2b) exhibiting varying hatch spacing and the *Velocity* sample (2c) exhibiting varying scan velocity.

(Fig. 2a) with each sample comprised of 10 separate steps and each step consisting of a 16 build layers with a 30 μm layer height. Within each of these steps a different combination of process parameters were implemented with changes to either hatch spacing (Fig. 2b) or scanning velocity (Fig. 2c). The expected dimensions of each sample are 4.80 mm \times 2.80 mm \times 1.00 mm in height, length, and width respectively.⁴⁹ Each step consisted of dimensions 0.48 mm in height and ranged from 1.00 mm to 2.80 mm in length, decreasing in length by 0.20 mm from the top of the sample to the bottom. The *Spacing* sample with varying hatch spacing was built with a constant 1.4 m/s scan velocity and the *Velocity* sample with varying scan velocity was built with a constant 50 μm hatch spacing.⁴⁹ A *normal* rastering pattern consisting of line scans parallel to the build axes, orthogonal to the previous layer was utilized as the scan strategy for both samples.

In-situ Pyrometry

Absolute temperature estimations were calculated from thermal radiation captured by a Stratronics two-color pyrometer receptive to light emitted at 750 nm and 900 nm, a frame rate within 6 - 7 kHz, and a 90 μs exposure.³³ Synchronization between the LPBF equipment

and pyrometer were achieved via Transistor-Transistor Logic (TTL) triggering producing 1000 frames of $65 \text{ px} \times 80 \text{ px}$ images within each build layer.³³ This translated to a $1365 \text{ }\mu\text{m} \times 1680 \text{ }\mu\text{m}$ resolution with approximately $21 \text{ }\mu\text{m}$ per px. This presented a total of 159,000 images taken for each sample and with initial screening applied to filter out "empty" images, reducing the total number of frames down to 20,469 and 20,187 for *Spacing* and *Velocity* samples respectively.

Ex-situ Micro-computed Tomography (CT)

Micro-computed tomography analysis was performed using a Zeiss Xradia 520 Versa at the maximum output power of 10 W and tube voltage of 140 kV with the sample positioned 11.1 mm from the source.⁴⁹ Scans were taken at a cubic voxel size of $3.63 \text{ }\mu\text{m}$ and with a build layer height of $30 \text{ }\mu\text{m}$, this equated to approximately 8.26 voxels per build layer. The obtained scans for the *Spacing* and *Velocity* samples were bounded by $5.05 \text{ mm} \times 3.00 \text{ mm} \times 1.35 \text{ mm}$ and $5.05 \text{ mm} \times 3.17 \text{ mm} \times 1.44 \text{ mm}$ respectively ($Z \times Y \times X$).⁴⁹ Both *Spacing* and *Velocity* samples extended $1410 \text{ voxels} \times 900 \text{ voxels} \times 430 \text{ voxels}$ along the Z, Y, and X axes. The scanned tomography was further segmented to distinguish each pore from the general sample with annotations denoting each of the labeled pore's centroid, equivalent diameter, number of voxels, and unique identifier.

Dataset

Pyrometry and Micro-computed Tomography Alignment

Capture area was limited to $80 \text{ px} \times 65 \text{ px}$ and lead to the raster patterns of the lower build layers (steps A - F) to extend further than the camera's viewport.³³ As mentioned, initial screening filtered out many of these empty frames by applying a minimum threshold on each frame's peak value from long wavelength data.³³ This method removed the frames where the melt pool was out of view, however still included some frames where spatter likely occurred.

In-situ thermal images and slices of *ex-situ* CT data shared the same origin at the top

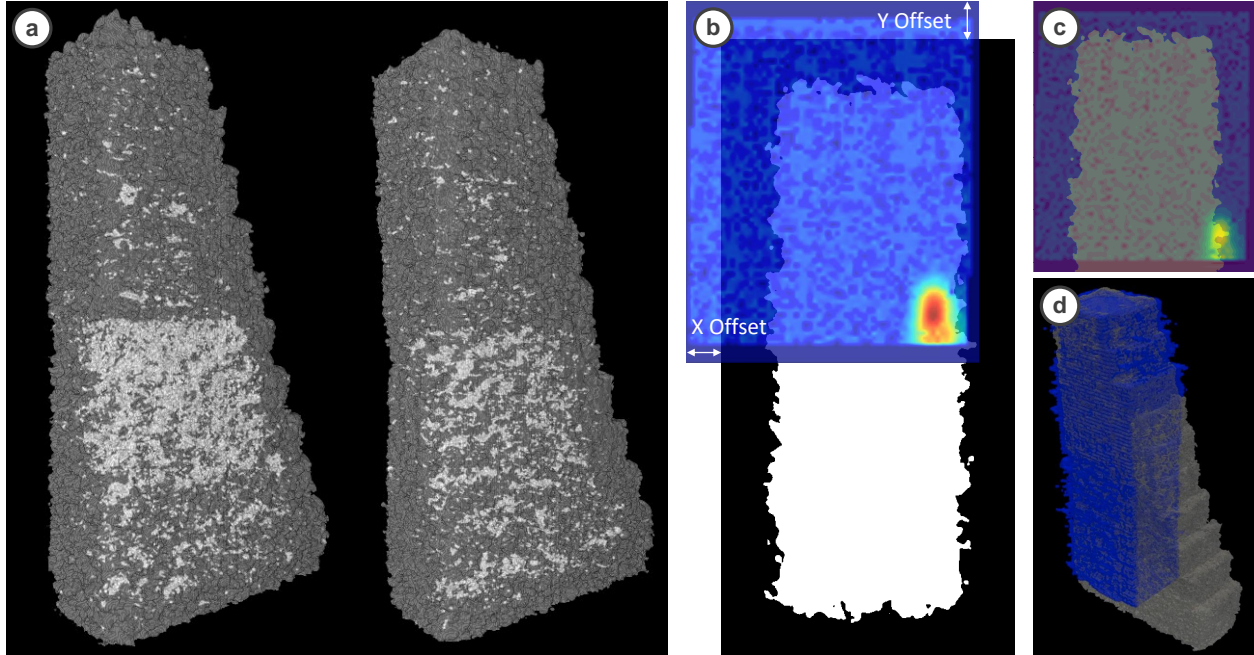


Figure 3: CT visualization of porosity segmented within overall sample for *Spacing* (left) and *Velocity* (right) samples (3a). Pyrometry data is captured within a subset of the built sample (3d) and initial alignment of image and CT data occurs along the X and Y axes (3b), using the top left corner of both as the origin. Alignment for a build layer is visually validated with an overlay of the pyrometry data directly on top of a corresponding cropped CT voxel layer (3c).

left (Fig 3 b). Small offsets were then applied to align the X and Y directions of CT to the thermal image. The provided Z direction offsets were used as starting points to align the CT data to the corresponding build layer. The Z alignment for both samples were visually verified through manual alignment of the scan path of thermal images and the a top down view of the corresponding CT layer. Step G (Fig. 2a) within both samples was the first section of the sample where the entire scan path is in complete view of the thermal camera and was used as a reference point to align the CT data. Both samples (*Spacing* and *Velocity*) were offset by a total 5 build layers (~9 voxels per build layer) in total.

Pore Thresholding

A CT resolution of 3.63 μm per voxel allowed for the capture of distinct shapes and contours associated with porosity, however this fine resolution also resulted in recording scattered distributions of small voids. Accurately predicting these small voids is a difficult task for a model as these defects could be the result of gas porosity⁵⁰ or rogue flaws⁵¹ and may have precursors not visible to thermal imaging. To achieve greater correlation between the pyrometry data and CT data, our attention focused on larger diameter pores that can be attributed to factors such as keyhole porosity or lack of fusion porosity. In keyholing, pores generated by the vapor column during builds resulted in an average diameter of 47 μm ⁵² and lack of fusion pores with diameters dependent on the height and width of melt pool and corresponding build layer.⁵³

The mean Equivalent Spherical Diameter (ESD) for each sample was compiled in order to obtain minimum threshold values 1 standard deviation above the mean. In the *Spacing* sample, pores exhibited an average diameter of 32.59 μm and a standard deviation of 20.60 μm , resulting in a minimum $(\mu + \sigma)$ ESD threshold of 53.19 μm . In the *Velocity* sample, pores had an average diameter of 30.78 μm and a smaller standard deviation of 16.01 μm resulting in a minimum $(\mu + \sigma)$ ESD thresholds of 46.79 (Fig. 4b).

Porosity Reconstruction

The quantity of pores and their position within the build layer was reconstructed with machine learning inferencing upon a sequence of thermal images. With the set of *in-situ* and *ex-situ* data, the tasks of predicting the number of pores and the approximate location of these pores within the various build layers were achieved using a CNN model and a ViViT model with dense prediction heads respectively.

The number of pores corresponding to a sequence of thermal images were predicted using a CNN model. In this task both the application of rotational transforms on the input

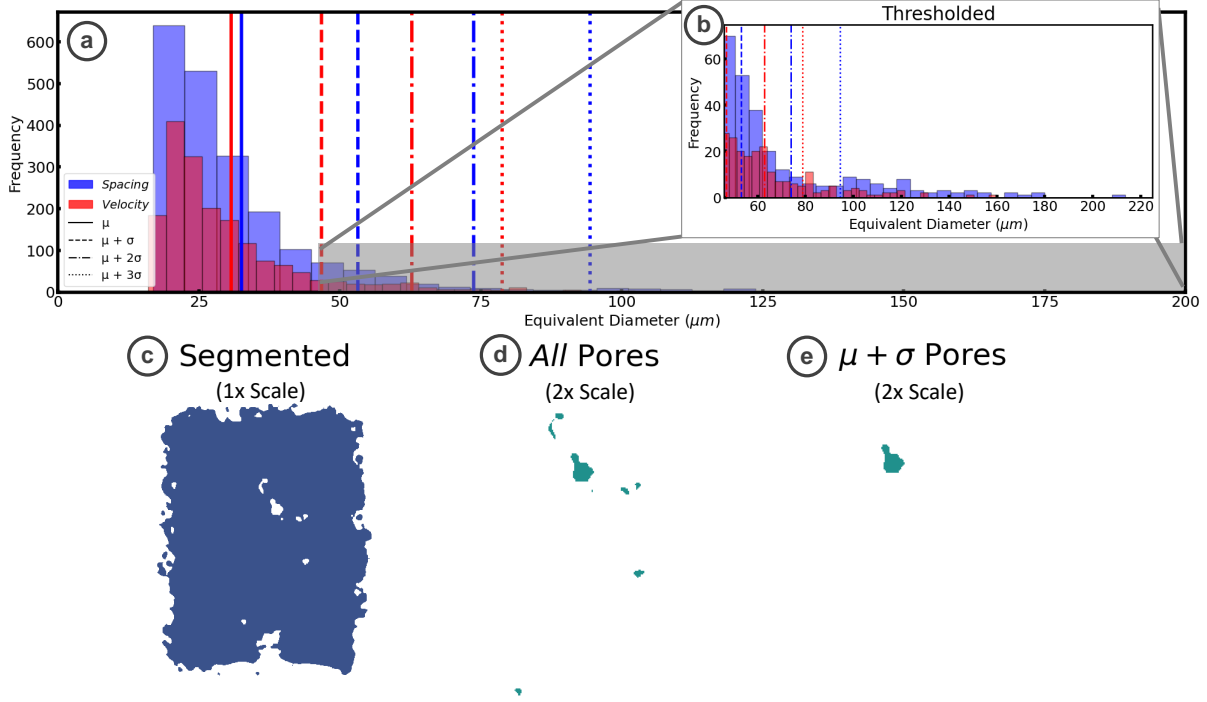


Figure 4: The *Spacing* sample on average consist of larger pores with a standard deviation of $20.5 \mu\text{m}$ compared to the *Velocity* sample’s standard deviation of $16.0 \mu\text{m}$ (4a). The tighter distribution of *Velocity* pores are visible in the thresholded distribution of equivalent pore sizes (4b) within the slices of the CT data. The segmentation of pores within the sample (4c) relied on a minimum of 100 voxels ($11.4 \mu\text{m}$ equivalent spherical diameter)³³ in order to register the contiguous cluster of voids as porosity (4d) and an increase in the minimum size further removed smaller pores (4e).

sequence and the volumetric depth utilized for pore count were treated as variables. Labels were derived from counting the set of unique pores within a specified volumetric depth corresponding to 1, 2 or 3 build layers and duplication was avoided by cross referencing each voxel’s pore id. The quality of these predictions is measured using Root Mean Square Error (RMSE) and R^2 score.

The localization of pores was predicted using the same sequence of thermal images and utilized a ViViT model with a dense prediction head to indicate sections expected to be porous. The labels for this task were obtained by downsampling the CT data for the build layer equally along all axes in order to provide a coarse porosity estimates for the model to train and predict. In addition, the effect of applying rotational transforms on the input sequence and minimum pore ESD thresholds for label compilation were investigated.

The quality of the predictions was measured using an Intersection over Union (IoU) score, considering the overlap of the area of predicted porosity over that of the label.

Porosity Count

This task investigates the extent in which sequences of thermal images can quantify the number of pores that exist within the sample build layers. The *Spacing* sample consists of 2069 pores and the *Velocity* sample consists of 1811 pores. The labels were obtained from slicing the CT sample data into the appropriate dimensions that corresponding to the build layer and counting the number of unique pore identifiers omitting the 0 value which represented the background. Each build layer consisted of 9 voxels in depth and this volume was extended to a depth of 18 and 27 voxels to obtain pore counts extending down 2 and 3 build layers.

In this task a CNN model composed of 4 convolutional layers and 2 fully connected layers reduce the input set of 200 64×64 pixel images into a scalar value of the number of unique pores within the build layer (Fig. 5). A 3×3 pixel kernel is convolved on top each image with a stride of 2 and a padding of 1. Within each layer the number of channels is reduced by a factor of 2 and batch normalization and ReLU non-linearity activation function are applied. The output of the CNN layers are reshaped into a 2 dimensional tensor before they are passed to the two fully connected layers which output a single scalar value which quantifies the number of pores within the build layer.

A CNN operates by leveraging convolutional layers to extract features from input images hierarchically. In the initial layers, low level features such as edges and gradients are detected through convolutional operations where the kernel moves across the input image, computing dot products and producing feature maps.^{42,43,54,55} Activation functions such as ReLU apply non-linear transforms and allow for the capture of complex patterns. The following layers then build upon these low level feature maps and repeat this task of transforming the raw pixel values into the outputs for a specific task.⁴² These tasks are determined by the final

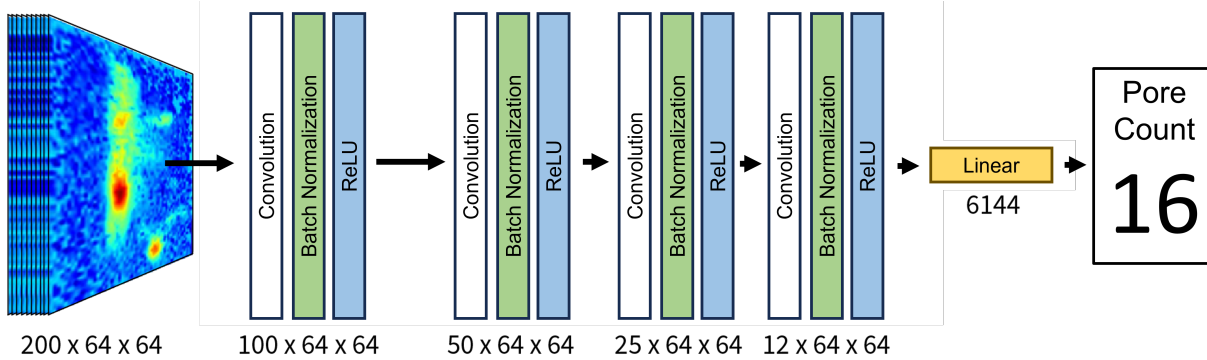


Figure 5: A standard convolutional neural network with a kernel size of 3 pixels and a stride of 2 filters the features within an image down over 4 layers to a singular scalar value indicating the expected number of pores from the sequence of thermal images.

layers of the network which utilize fully connected layers to shape the output to perform classification, regression, or reconstruction.

Due to dataset size constraints, a 75 / 25 train test split of the data was used for model training. The train test split occurred within the 16 build layers of each of the 10 sample steps of either the *Spacing* or *Velocity* sample. This split within sample steps was implemented to provide an equal distribution of processing parameters between the train and test sets for the model. This provided an input label set of 120 training pairs and 39 testing pairs for the either of the samples. Our dataset implementation allowed for the model to train on either the *Spacing*, *Velocity*, or on a combination of both datasets with the *All* dataset. For this regression task, a mean squared error was utilized as the loss function and the predicted value from the model is rounded to the nearest integer. Each of the models were trained from 500 epochs with a learning rate of 0.0001 using the ADAM optimizer.

In addition, data augmentations of the input sequence in the form of rotational transforms for the entire video sequence were applied. Data augmentation provides a means to artificially expand an existing set of data in order to improve the generalization ability and robustness of the model.⁴² Typical transformations change the input image applying one or a combination of rotations, translations, flips, scaling, and cropping. In this application we focus only on applying rotational transforms ranging between 0° to 180° and avoid alterations to the

contrast or brightness that would affect the raw temperature value.

Porosity Localization

The localization task identifies areas within the build layer where pores are likely to form through analyzing a sequence of thermal images. A video vision transformer (ViViT) provides an applicable architecture to thoroughly analyze the series of input frames to extract positional features through use of spatial and temporal attention.⁴⁴ In our model implementation a sequence of thermal images is provided to the model to map to localized porosity labels obtained through alignment and extraction of the CT data. These build layers of initial size of $9 \times 423 \times 520$ voxels are cropped and downsampled by a factor of 24 to a coarser 2 dimensional $1 \times 16 \times 16$ voxel shape to provide a general area in which porosity is expected.

For this task a video vision transformer model with a dense prediction output is utilized to localize pores within the sample space. This model is composed of a spatial transformer layer with 4 sub-layers and a temporal transformer layer with 5 sub-layers both with 8 heads and a dimension of 256 (Fig. 6). Afterwards the class tokens resulting from each of the transformer layers are removed and the output is passed into a feature fusion block which performs residual convolution and provide a fine grain prediction. A series of 4 convolutional layers and ReLU non-linearity layers are applied before passing to a sigmoid activation function to indicate whether porosity is expected at a voxel location.

Attention within a transformer is comprised of three learnable components: The query vector $\{\mathbf{q}_i\}_{i=1}^{N_q}$, key vector $\{\mathbf{k}_i\}_{i=1}^{N_k}$, and the value vector $\{\mathbf{v}_i\}_{i=1}^{N_v}$ given that $N_k = N_v$.⁵⁶⁻⁵⁸ In the attention mechanism, the query vector retrieves contextual information from the key vector and generates an output based on the weighted sum of corresponding value vectors. Contextual information is retrieved in the form of an attention score which is the scaled dot product between the query vector and the key vector: $\frac{\mathbf{q}_i \cdot \mathbf{k}_j^T}{\sqrt{d}}$.⁵⁷ The attention score is then used in the calculation of weights (α_{ij}) which apply a Softmax over the individual

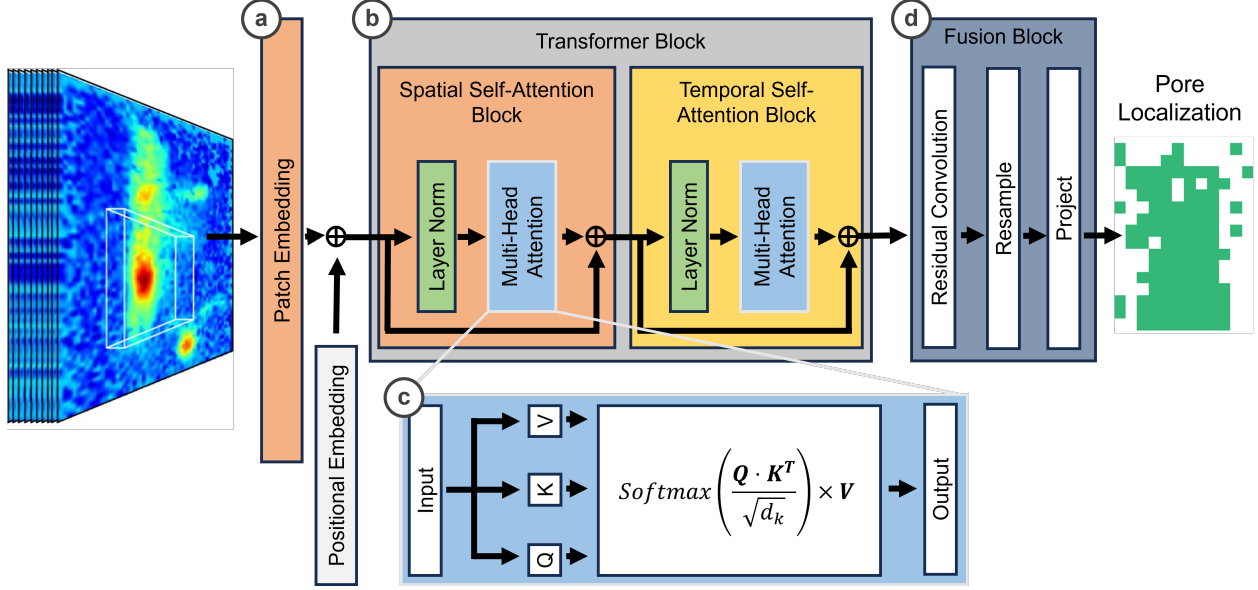


Figure 6: The input sequence of thermal images are sliced into a set of patches (6a) where 4 and 5 sublayers of the respective spatial and temporal self attention are applied (6b). Each self attention block consisted of 8 attention heads (6c) of a dimension of 256. A feature fusion block (6d) applies residual convolution and a dense prediction head produces a 2 dimensional output indicating regions of expected porosity.

contribution of each attention score (Eq. 1).⁵⁶⁻⁵⁸ Each token's numerical encoding along with its relevance to other tokens is calculated from the cross product between the value vector and weights resulting in the attention mechanism: $Softmax\left(\frac{\mathbf{Q} \cdot \mathbf{K}^T}{\sqrt{d_k}}\right) \times V$.⁵⁶⁻⁵⁸

$$\alpha_{ij} = Softmax\left(\frac{e^{\frac{\mathbf{q}_i \cdot \mathbf{k}_j^T}{\sqrt{d}}}}{\sum_{k=1}^N e^{\frac{\mathbf{q}_i \cdot \mathbf{k}_j^T}{\sqrt{d}}}}\right) = Softmax\left(\frac{\mathbf{Q} \cdot \mathbf{K}^T}{\sqrt{d_k}}\right) \quad (1)$$

In the case of a Vision Transformer (ViT), an image is divided up into self attention patches via patch embedding, passed through the transformer encoder, and utilized through a classification head.^{44,59} Within patch embedding, each patch has a fixed pixel size in height and width and its embedding is derived through flattening and linear projection.^{44,59} Class and position are applied to the embedding before passed through the transformer encoder composed blocks of layer norm, multi-head attention, and MLP layers after which a classification head is attached.⁵⁹

The dataset utilizes the same 75 / 25 train test split within the sample steps for all the

Spacing, *Velocity*, and *All* variants. The model was trained for 1000 epochs utilizing a binary cross entropy loss function for the binary prediction of a voxel’s porosity classification. An ADAM optimizer along with a cosine decay learning rate scheduler with an initial 10 epoch warm up period from learning rates 0.00001 to 0.0001 is applied to help with regularization and stabilization.⁶⁰

Results and Discussion

Porosity Count

The number of pores within a volume of the sample was predicted from a sequence of thermal images using a CNN model trained on either the *Spacing*, *Velocity*, or *All* dataset. Hyperparameters such as the utilization of rotational transforms and the number of build layers involved in the compilation of the pore count were investigated.

Table 1 outlines the model’s performance according to its training dataset and indicates the data augmentation procedures that were applied and the various depths used to calculate pore count. Models with datasets spanning 1 build layer exhibited the lowest error and highest R^2 with a minimum RMSE score of 7.84 from the *Velocity* sample and a maximum R^2 score of 0.57 from the *Spacing* sample. The RMSE and R^2 score aim to measure the average magnitude of errors and capture the proportion of variance within the model respectively. The alignment of the prediction and the corresponding target for each model (Fig. 7) shows a general trend where there is a larger degree of porosity within the build layers ranging from 60 to 100 and to a lesser degree elsewhere. Notably, build layers greater than 100 display lower amounts of porosity for all models regardless of dataset or data augmentation.

This is expected as both samples transition from off nominal process parameters to nominal process parameters towards the middle of the sample (Table 2b, 2c) with the upper portion of each sample fabricated with ideal process parameters. For all models, areas where the sample was fabricated with nominal process parameters show a greater degree

of clustering as pores are sparse and few. In earlier build layers, specifically those closer towards the middle of the sample a greater spread of predictions is seen (Fig. 7b, 7e, 7f).

The model trained with the *Spacing* dataset without rotational transforms (Fig. 7a) achieved the highest R^2 score of all models with a score of 0.57. This indicates that the more than half of the variance within this model is able to be explained by the input data. However, the model trained with the *Velocity* sample and rotational transforms achieved the lowest RMSE score of 7.84 of all models on input data with significantly less variability as indicated with their lower R^2 scores. The model trained on the *All* dataset produced RMSE and R^2 scores inbetween that of models trained on either *Spacing* or *Velocity* datasets except in the situation for the case where rotational transforms were applied where it yielded a R^2 score of 0.07. The additional hyperparameter of various build layer depths displayed worse RMSE and R^2 scores indicating that there exists a greater correlation between the thermal images and the build layer directly underneath it.

The RMSE and R^2 values align with what is expected of the two *Spacing* and *Velocity* datasets as the hatch spacing and scan velocity are the two variables that change between sample steps respectively. In the case of *Spacing* sample, the hatch spacing produces a visible signal in the form total rasters that is visible over the sequence of input frames. However, the *Velocity* sample uses a consistent number of rasters traveling both vertically and horizontally across the build plate. The most significant visual signal in the *Velocity* sample is the distance the melt pool travels inbetween frames.

Table 1: R^2 and RMSE prediction performance metrics for CNN model trained on various datasets and build layer depths for 500 epochs.

| Dataset | Data Augmentation | 1 Build Layer | | 2 Build Layers | | 3 Build Layers | |
|-----------------|-------------------|---------------|-------------|----------------|-------------|----------------|-------------|
| | | RMSE | R^2 | RMSE | R^2 | RMSE | R^2 |
| <i>Spacing</i> | Rotational | 12.60 | 0.33 | 19.04 | 0.18 | 22.94 | 0.17 |
| | None | 10.14 | 0.57 | 18.46 | 0.23 | 19.75 | 0.39 |
| <i>Velocity</i> | Rotational | 7.84 | 0.09 | 11.41 | -0.04 | 14.74 | 0.03 |
| | None | 8.08 | 0.03 | 8.95 | 0.36 | 13.25 | 0.22 |
| <i>All</i> | Rotational | 11.90 | 0.07 | 13.89 | 0.34 | 17.81 | 0.26 |
| | None | 9.73 | 0.38 | 14.57 | 0.27 | 16.88 | 0.34 |

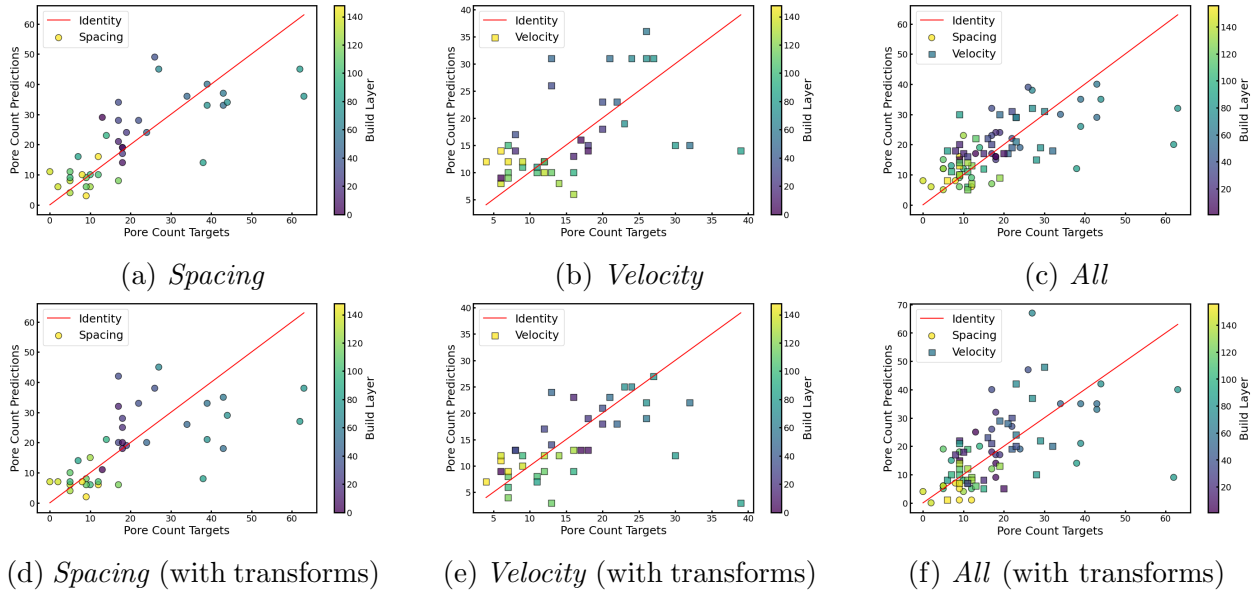


Figure 7: CNN pore count predictions plotted alongside target pore values for *Spacing*, *Velocity*, and *All* (combination of both datasets) for a depth of 1 build layer. In all plots the pore counts for build layers 100 - 160 are clustered near the origin as the upper half of the sample is composed of nominal process conditions. Of all the various implementations, the CNN model trained on the *Spacing* (Fig. 7a) dataset without transforms shows the greatest level of alignment between the prediction and ground truth.

Porosity Localization

During the training process, rotation transforms of the entire video sequence were introduced as data augmentation methods and compared against models trained without any rotational transformations. In addition to data augmentations, the datasets were adjusted to allow for training on *All Pores* and on pores with ESD 1 standard deviation above the mean ($\mu + \sigma$ *Pores*) in an effort to investigate the model’s performance on identifying the larger pores within the dataset.

The position of the pores within the build layer was predicting using a sequence of thermal images with the ViViT Dense model trained on either the *Spacing*, *Velocity*, and *All* dataset. The effect of data augmentation and applying a threshold for minimum ESD for pores were investigated with the training of this model as well. The Intersection over Union (IoU) also known as the Jaccard Index was used to quantify the performance of each model’s prediction. The intersection over union quantifies the prediction area overlap onto

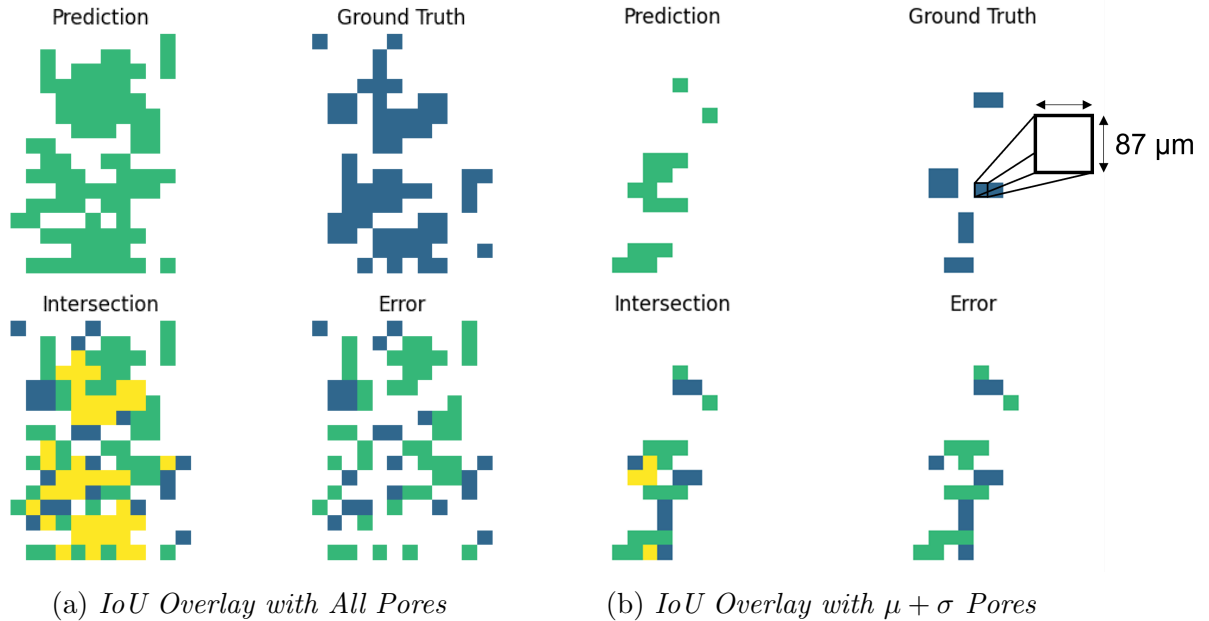


Figure 8: Comparison of prediction and label values for the model trained on the *All* sample alongside the application of a minimum ESD pore threshold (Fig. 8b). The areas colored in yellow represent the intersection that is considered for IoU calculations.

the target with the highest metric of 1.0 occurring from an exact overlap of the two sets. For the IoU calculation each set only includes the areas of porosity and in the case where both the target and prediction exhibited no porosity, a score of 1.0 was given as the prediction provided an exact match of the ground truth.

The effect of training on the various *Spacing*, *Velocity*, and *All* datasets were investigated for this task as well the impact of rotational transforms on the input sequence. In addition, the prediction performance of the model upon applying a threshold to hide pores smaller than 1 standard deviation above the mean was applied. The prediction results of these models measured for each input label pair within the test dataset with the overall average and maximum IoU scores recorded on Table 2. Within the datasets that included *All Pores*, models trained on the *Spacing* datasets performed the best on average IoU scores when trained without rotational transforms. A maximum IoU score of 0.85 was achieved within the model trained on the dataset for *All* samples with rotational transforms applied. Without the applied threshold for minimum pore ESD, the model trained on the *Velocity* produces

the lowest IoU score of the three models. However, after a minimum pore ESD threshold is applied, the *Velocity* dataset model performs on par to that of the model trained with the *Spacing* dataset. In all of the cases there was a greater trend in overlap within the lower layers of the sample (Fig. 8a) likely due to the higher porosity resulting from the off nominal process conditions used within those sample steps.

With a minimum pore threshold of 1 standard deviation above the mean pore equivalent diameter ($\mu + \sigma$ Pores), all models were able to achieve maximum IoU scores of 1. These results were achieved towards the top of each sample where nominal process conditions were used and correctly predicted the ground truth of no pores above the threshold were present. (Fig. 8b) In some cases, areas with higher levels of porosity produced lower IoU scores after thresholding as the previously larger regions associated with porosity are reduced in size (Fig. 8). Overall, the mean IoU increased for all models after the application of a minimum pore ESD threshold. The greatest of these increases is seen in the models trained with the *All* dataset of which scored the highest average IoU of any other models. Rotational transforms did not prove to have a significant impact on improving training as the resulting metrics were often within a percent error from each other.

Table 2: Pore localization prediction performance metrics for ViViT Dense model trained on *Spacing*, *Velocity*, and *All* sample datasets for 1000 epochs on both all segmented pores and pores with equivalent diameters greater than 1 standard deviation above the mean. The adjusted threshold to consider only pores with larger equivalent diameters improved prediction results in build layers with nominal process parameter and low resulting porosity.

| Dataset | Data Augmentation | <i>All Pores</i> | | $\mu + \sigma$ Pores | |
|-----------------|-------------------|------------------|-------------|----------------------|------------|
| | | Average IoU | Max IoU | Average IoU | Max IoU |
| <i>Spacing</i> | Rotational | 0.25 | 0.75 | 0.29 | 1.0 |
| | None | 0.28 | 0.77 | 0.28 | 1.0 |
| <i>Velocity</i> | Rotational | 0.16 | 0.42 | 0.24 | 1.0 |
| | None | 0.17 | 0.44 | 0.29 | 1.0 |
| <i>All</i> | Rotational | 0.22 | 0.85 | 0.32 | 1.0 |
| | None | 0.21 | 0.72 | 0.32 | 1.0 |

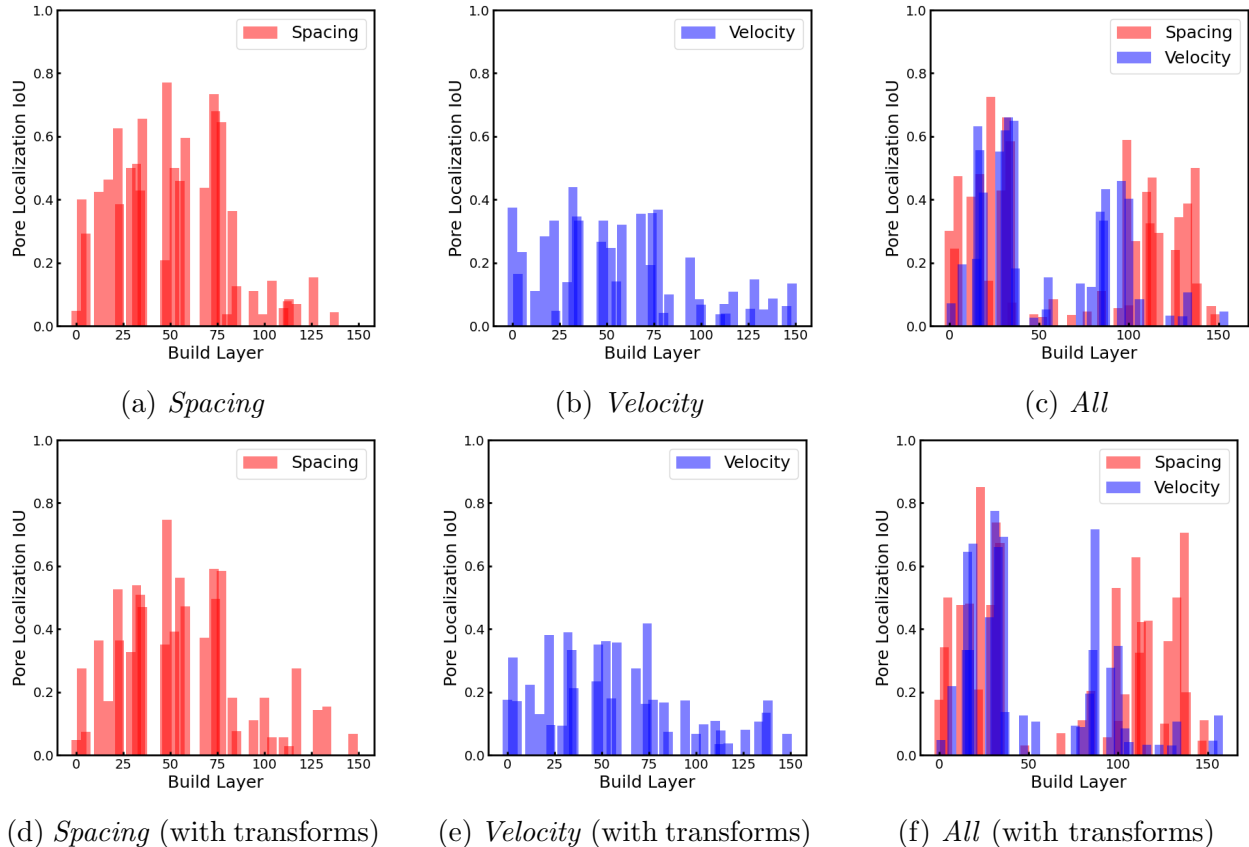


Figure 9: IoU trends by build layer for various datasets with and without rotational transforms.

Conclusion and Future Work

In this work we investigate the application of machine learning to *in-situ* thermal image process monitoring for the prediction of pore count and pore localization. For this we utilized a CNN architecture and a modified ViViT model with dense prediction heads for various dataset such as *Spacing*, *Velocity*, and *All*. For the task of pore quantification, we have found that the *Spacing* dataset provides the greatest amount of signal within and models trained on the *Velocity* dataset produces the least amount of error. The pore localization task displayed a similar trend with models trained on the *Spacing* dataset achieving the best overlap when evaluating *All Pores*. The model trained on the *All* dataset showed better performance when evaluating on $\mu + \sigma$ *Pores*.

In both tasks, the effect of rotational transforms were minimal resulting in a negligible

difference in prediction outcomes. Our pore localization model experienced improved performance with the application of a minimum pore ESD threshold as it achieved higher average IoU scores, especially within areas of the sample built with nominal processing parameters. These works show the potential of utilizing *in-situ* process monitoring techniques for faster *ex-situ* part certification and future work would aim to develop a more robust digital twin achieving greater defect quantification and localization precision over the entire sample.

Acknowledgement

Sandia National Laboratories is a multimission laboratory managed and operated by National Technology & Engineering Solutions of Sandia, LLC, a wholly owned subsidiary of Honeywell International Inc., for the U.S. Department of Energy’s National Nuclear Security Administration under contract DE-NA0003525. This paper describes objective technical results and analysis. Any subjective views or opinions that might be expressed in the paper do not necessarily represent the views of the U.S. Department of Energy or the United States Government.

Supporting Information Available

Input Cropping and Label Downsampling

The input thermal images were cropped from the original 85 px \times 60 px shape down to a 64 px \times 64 px shape to fit the desired input shape of the network. To achieve this 8 pixels (188.8 μm) were cropped from both the top and bottom of the image and 1 pixel (23.6 μm) was removed from the left hand side of the image. To match the cropped input, the corresponding CT label was first cropped then downsampled to align with the expected 64 px \times 64 px input. The crops of 8 pixels and 1 pixel were converted to their voxel equivalents and rounded to 52 voxels and 7 voxels respectively. This reduced the CT label a size of 520

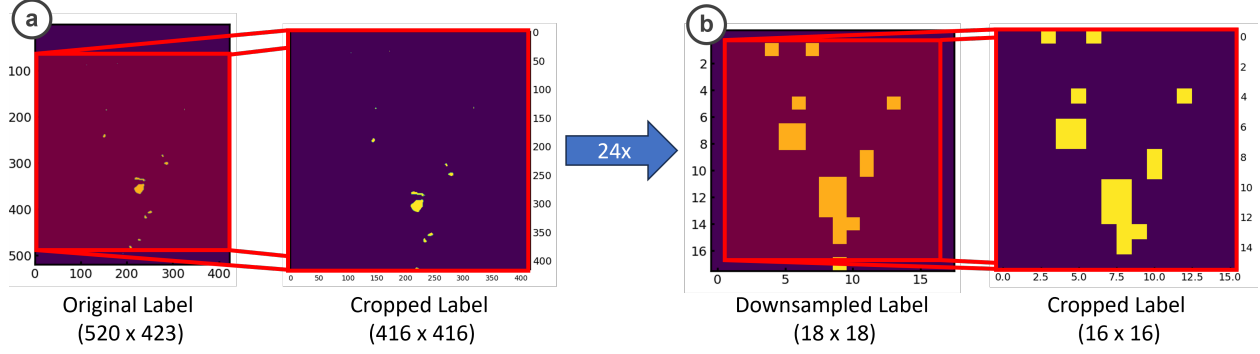


Figure 10: Relative porosity locations are derived from the raw CT data which are cropped to capture a consistent area to match the input thermal data (Fig. 10a). The CT data is further downsampled factor of 24 and cropped to provide a 16 x 16 label shape (Fig. 10b).

voxels \times 423 voxels down to 416 voxels \times 416 voxels (Fig. 10a). The resulting cropped CT was downsampled by a factor of 24 down to 18 voxels \times 18 voxels along the x and y directions and 1 voxel along the z direction. Further cropping was applied to the x and y directions by 1 voxel on each side to reduce the label down to 16 voxels \times 16 voxels \times 1 voxel (Fig. 10b).

Calculating absolute temperature estimations with data obtained through Stratonics pyrometer

The estimation of absolute temperature was achieved with grey-body assumption where the emissivity remains constant at various wavelengths. Thus, with proper calibration using a NIST-traceable tungsten lamp, the pyrometer was able to read out a temperature estimation within 4% accuracy for stainless steel.³³ This temperature is estimated with the following formula for hybrid mode temperature estimation (Eq. 2) where p_2 is a constant held at 14388 nm-K. Wien's approximation⁶¹ of Planck's law is used to evaluate A_λ (Eq. 3) which takes into consideration emissivity and the instrument's detection factor with \bar{I}_1 representing the average intensity calculated over region Ω_p . I_1 and I_2 here represent the the radiance from images over Ω_p , for $\lambda_1 = 750\text{nm}$ and $\lambda_2 = 900\text{nm}$ respectively. The temperature ratio T_R (Eq. 4) is calculated with R , the average of radiance from images I_1 and I_2 over Ω_p , and hardware

constants for contour levels c_1 and c_2 obtained from least squares fitting over calibration data.⁶² Contour level defines the region Ω_p with a β value between 0 and 1 through means of marching squares (Eq. 5). Our dataset utilizes images taken at $\beta = 0.7$ for its most accurate approximation of the meltpool by single contour as opposed to the multiple contours that appear at $\beta = 0.3$.

$$T_H = \frac{p_2}{\lambda_2 \ln(A_\lambda/I_2)} \quad (2)$$

$$A_\lambda = \bar{I}_1 e^{p_2/\lambda_1 T_R} \quad (3)$$

$$T_R = \frac{1}{c_1 \ln R + c_2} \quad (4)$$

$$c = \beta \times \max(I) \quad (5)$$

Sample alignment of thermal images to CT data along the X and Y axes

CT data for both samples had a shape of $1410 \times 900 \times 430$ voxels with values ranging from 0 - 255 depending on data selection type of pore, sample, or pore segmented sample. Common alignment between the *in-situ* pyrometry data and *ex-situ* CT data was established by converting the pyrometry data into voxels and applying a consistent offset. The *in-situ* pyrometry data was converted from pixels ($80 \text{ px} \times 65 \text{ px}$) to microns ($1680 \text{ }\mu\text{m} \times 1365 \text{ }\mu\text{m}$) to voxels ($462.81 \text{ voxels} \times 376.03 \text{ voxels}$). The CT data was then shifted to align with the pyrometry data by $-18 \text{ voxels} \times 0 \text{ voxels} \times 63 \text{ voxels}$ for the *Spacing* dataset and $-14 \text{ voxels} \times -2 \text{ voxels} \times 73 \text{ voxels}$ for the *Velocity* dataset.

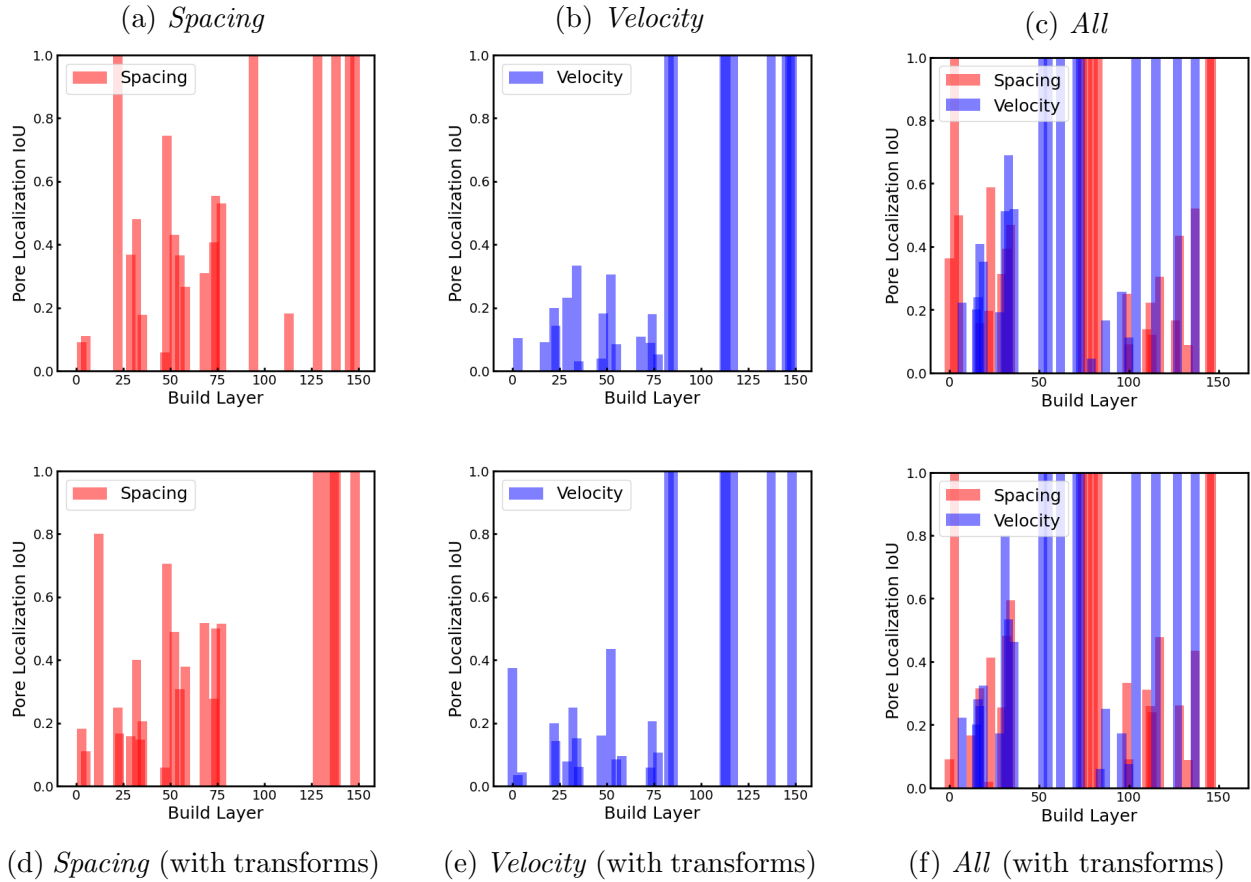


Figure 11: IoU trends by build layer for various datasets with and without rotational transforms with the application of minimum equivalent diameter pore threshold.

IoU scores of models trained on equivalent sphere diameter pores

1 standard deviation above the mean ($\mu + \sigma$ Pores)

References

- (1) Rahman, M. A.; Saleh, T.; Jahan, M. P.; McGarry, C.; Chaudhari, A.; Huang, R.; Tauhiduzzaman, M.; Ahmed, A.; Mahmud, A. A.; Bhuiyan, M. S.; Khan, M. F.; Alam, M. S.; Shakur, M. S. Review of Intelligence for Additive and Subtractive Manufacturing: Current Status and Future Prospects. *Micromachines* **2023**, *14*, 508, Number: 3 Publisher: Multidisciplinary Digital Publishing Institute.
- (2) Beaman, J. J.; Bourell, D. L.; Seepersad, C. C.; Kovar, D. Additive Manufacturing

- Review: Early Past to Current Practice. *Journal of Manufacturing Science and Engineering* **2020**, *142*.
- (3) Akbari, P.; Ogoke, F.; Kao, N.-Y.; Meidani, K.; Yeh, C.-Y.; Lee, W.; Barati Farimani, A. MeltpoolNet: Melt pool characteristic prediction in Metal Additive Manufacturing using machine learning. *Additive Manufacturing* **2022**, *55*, 102817.
- (4) Hemmasian, A.; Ogoke, F.; Akbari, P.; Malen, J.; Beuth, J.; Barati Farimani, A. Surrogate modeling of melt pool temperature field using deep learning. *Additive Manufacturing Letters* **2023**, *5*, 100123.
- (5) Ordás, N.; Ardila, L. C.; Iturriza, I.; Garcíanda, F.; Álvarez, P.; García-Rosales, C. Fabrication of TBMs cooling structures demonstrators using additive manufacturing (AM) technology and HIP. *Fusion Engineering and Design* **2015**, *96-97*, 142–148.
- (6) Dolimont, A.; Michotte, S.; Rivière-Lorphèvre, E.; Ducobu, F.; de Formanoir, C.; Godet, S.; Filippi, E. Effect of HIPping (Hot Isostatic Pressing) on electron beam melting Ti6Al4V parts after machining. *AIP Conference Proceedings* **2016**, *1769*, 190006.
- (7) Knapp, G. L.; Mukherjee, T.; Zuback, J. S.; Wei, H. L.; Palmer, T. A.; De, A.; DebRoy, T. Building blocks for a digital twin of additive manufacturing. *Acta Materialia* **2017**, *135*, 390–399.
- (8) Bartsch, K.; Pettke, A.; Hübert, A.; Lakämper, J.; Lange, F. On the digital twin application and the role of artificial intelligence in additive manufacturing: a systematic review. *Journal of Physics: Materials* **2021**, *4*, 032005, Publisher: IOP Publishing.
- (9) Gaikwad, A.; Yavari, R.; Montazeri, M.; Cole, K.; Bian, L.; Rao, P. Toward the digital twin of additive manufacturing: Integrating thermal simulations, sensing, and analytics to detect process faults. *IISE Transactions* **2020**, *52*, 1204–1217, Publisher: Taylor & Francis _eprint: <https://doi.org/10.1080/24725854.2019.1701753>.

- (10) Clymer, D. R.; Cagan, J.; Beuth, J. Power–Velocity Process Design Charts for Powder Bed Additive Manufacturing. *Journal of Mechanical Design* **2017**, *139*.
- (11) Agrawal, A. K.; Rankouhi, B.; Thoma, D. J. Predictive process mapping for laser powder bed fusion: A review of existing analytical solutions. *Current Opinion in Solid State and Materials Science* **2022**, *26*, 101024.
- (12) Grasso, M.; Remani, A.; Dickins, A.; Colosimo, B. M.; Leach, R. K. In-situ measurement and monitoring methods for metal powder bed fusion: an updated review. *Measurement Science and Technology* **2021**, *32*, 112001, Publisher: IOP Publishing.
- (13) Xia, M.; Gu, D.; Yu, G.; Dai, D.; Chen, H.; Shi, Q. Influence of hatch spacing on heat and mass transfer, thermodynamics and laser processability during additive manufacturing of Inconel 718 alloy. *International Journal of Machine Tools and Manufacture* **2016**, *109*, 147–157.
- (14) Snyder, J. C.; Stimpson, C. K.; Thole, K. A.; Mongillo, D. J. Build Direction Effects on Microchannel Tolerance and Surface Roughness. *Journal of Mechanical Design* **2015**, *137*.
- (15) Mertens, R.; Clijsters, S.; Kempen, K.; Kruth, J.-P. Optimization of Scan Strategies in Selective Laser Melting of Aluminum Parts With Downfacing Areas. *Journal of Manufacturing Science and Engineering* **2014**, *136*.
- (16) Gockel, J.; Beuth, J. Understanding Ti-6Al-4V Microstructure Control in Additive Manufacturing via Process Maps. **2013**, Publisher: University of Texas at Austin.
- (17) Slotwinski, J. A.; Garboczi, E. J.; Hebenstreit, K. M. Porosity Measurements and Analysis for Metal Additive Manufacturing Process Control. *Journal of Research of the National Institute of Standards and Technology* **2014**, *119*, 494–528.
- (18) Measurement Science Roadmap for Metal-Based Additive Manufacturing.

- (19) Tian, X.; Wu, L.; Gu, D.; Yuan, S.; Zhao, Y.; Li, X.; Ouyang, L.; Song, B.; Gao, T.; He, J.; Lin, X.; Lin, F.; Zhu, J.; Li, D. Roadmap for Additive Manufacturing: Toward Intellectualization and Industrialization. *Chinese Journal of Mechanical Engineering: Additive Manufacturing Frontiers* **2022**, *1*, 92.
- (20) Biegler, M.; Graf, B.; Rethmeier, M. In-situ distortions in LMD additive manufacturing walls can be measured with digital image correlation and predicted using numerical simulations. *Additive Manufacturing* **2018**, *20*, 101–110.
- (21) Hofman, J.; Wudy, K. In situ process monitoring in laser-based powder bed fusion of polyamide 12 using thermal imaging. *The International Journal of Advanced Manufacturing Technology* **2022**, *122*, 4127–4138.
- (22) Ren, Z.; Gao, L.; Clark, S. J.; Fezzaa, K.; Shevchenko, P.; Choi, A.; Everhart, W.; Rollett, A. D.; Chen, L.; Sun, T. Machine learning–aided real-time detection of key-hole pore generation in laser powder bed fusion. *Science* **2023**, *379*, 89–94, Publisher: American Association for the Advancement of Science.
- (23) Tempelman, J. R.; Wachtor, A. J.; Flynn, E. B.; Depond, P. J.; Forien, J.-B.; Guss, G. M.; Calta, N. P.; Matthews, M. J. Detection of keyhole pore formations in laser powder-bed fusion using acoustic process monitoring measurements. *Additive Manufacturing* **2022**, *55*, 102735.
- (24) McCann, R.; Obeidi, M. A.; Hughes, C.; McCarthy, E.; Egan, D. S.; Vijayaraghavan, R. K.; Joshi, A. M.; Acinas Garzon, V.; Dowling, D. P.; McNally, P. J.; Brabazon, D. In-situ sensing, process monitoring and machine control in Laser Powder Bed Fusion: A review. *Additive Manufacturing* **2021**, *45*, 102058.
- (25) Feng, S.; Chen, Z.; Bircher, B.; Ji, Z.; Nyborg, L.; Bigot, S. Predicting laser powder bed fusion defects through in-process monitoring data and machine learning. *Materials & Design* **2022**, *222*, 111115.

- (26) Seifi, M.; Salem, A.; Beuth, J.; Harrysson, O.; Lewandowski, J. J. Overview of Materials Qualification Needs for Metal Additive Manufacturing. *JOM* **2016**, *68*, 747–764.
- (27) Chen, Z.; Han, C.; Gao, M.; Kandukuri, S. Y.; Zhou, K. A review on qualification and certification for metal additive manufacturing. *Virtual and Physical Prototyping* **2022**, *17*, 382–405, Publisher: Taylor & Francis _eprint: <https://doi.org/10.1080/17452759.2021.2018938>.
- (28) Dordlofva, C. A Design for Qualification Framework for the Development of Additive Manufacturing Components—A Case Study from the Space Industry. *Aerospace* **2020**, *7*, 25, Number: 3 Publisher: Multidisciplinary Digital Publishing Institute.
- (29) Sola, A.; Nouri, A. Microstructural porosity in additive manufacturing: The formation and detection of pores in metal parts fabricated by powder bed fusion. *Journal of Advanced Manufacturing and Processing* **2019**, *1*, e10021, _eprint: <https://onlinelibrary.wiley.com/doi/pdf/10.1002/amp2.10021>.
- (30) Myers, A. J.; Quirarte, G.; Ogoke, F.; Lane, B. M.; Uddin, S. Z.; Farimani, A. B.; Beuth, J. L.; Malen, J. A. High-resolution melt pool thermal imaging for metals additive manufacturing using the two-color method with a color camera. *Additive Manufacturing* **2023**, *73*, 103663, Publisher: Elsevier.
- (31) Kayacan, M. Y.; Yilmaz, N. An investigation on the measurement of instantaneous temperatures in laser assisted additive manufacturing by thermal imagers. *Measurement* **2020**, *160*, 107825.
- (32) Haley, J.; Leach, C.; Jordan, B.; Dehoff, R.; Paquit, V. In-situ digital image correlation and thermal monitoring in directed energy deposition additive manufacturing. *Optics Express* **2021**, *29*, 9927–9941, Publisher: Optica Publishing Group.
- (33) Mitchell, J. A.; Ivanoff, T. A.; Dagel, D.; Madison, J. D.; Jared, B. Linking pyrometry to porosity in additively manufactured metals. *Additive Manufacturing* **2020**, *31*, 100946.

- (34) Borish, M.; Post, B. K.; Roschli, A.; Chesser, P. C.; Love, L. J. Real-Time Defect Correction in Large-Scale Polymer Additive Manufacturing via Thermal Imaging and Laser Profilometer. *Procedia Manufacturing* **2020**, *48*, 625–633.
- (35) Borish, M.; Post, B. K.; Roschli, A.; Chesser, P. C.; Love, L. J.; Gaul, K. T.; Sallas, M.; Tsiamis, N. In-Situ Thermal Imaging for Single Layer Build Time Alteration in Large-Scale Polymer Additive Manufacturing. *Procedia Manufacturing* **2019**, *34*, 482–488.
- (36) Rosenthal, D. Mathematical Theory of Heat Distribution during Welding and Cutting. **1941**, *20*, 220s–234s.
- (37) Hekmatjou, H.; Zeng, Z.; Shen, J.; Oliveira, J. P.; Naffakh-Moosavy, H. A Comparative Study of Analytical Rosenthal, Finite Element, and Experimental Approaches in Laser Welding of AA5456 Alloy. *Metals* **2020**, *10*, 436, Number: 4 Publisher: Multidisciplinary Digital Publishing Institute.
- (38) Imani Shahabad, S.; Karimi, G.; Toyserkani, E. An Extended Rosenthal’s Model for Laser Powder-Bed Fusion Additive Manufacturing: Energy Auditing of Thermal Boundary Conditions. *Lasers in Manufacturing and Materials Processing* **2021**, *8*, 288–311.
- (39) Baturynska, I.; Semeniuta, O.; Martinsen, K. Optimization of Process Parameters for Powder Bed Fusion Additive Manufacturing by Combination of Machine Learning and Finite Element Method: A Conceptual Framework. *Procedia CIRP* **2018**, *67*, 227–232.
- (40) Ogoke, F.; Liu, Q.; Ajenifujah, O.; Myers, A.; Quirarte, G.; Beuth, J.; Malen, J.; Farimani, A. B. Inexpensive High Fidelity Melt Pool Models in Additive Manufacturing Using Generative Deep Diffusion. 2023; <http://arxiv.org/abs/2311.16168>, arXiv:2311.16168 [cond-mat].
- (41) Zhan, Z.; Li, H. Machine learning based fatigue life prediction with effects of additive

- manufacturing process parameters for printed SS 316L. *International Journal of Fatigue* **2021**, *142*, 105941.
- (42) Krizhevsky, A.; Sutskever, I.; Hinton, G. E. ImageNet classification with deep convolutional neural networks. *Communications of the ACM* **2017**, *60*, 84–90.
- (43) Tran, D.; Bourdev, L.; Fergus, R.; Torresani, L.; Paluri, M. Learning Spatiotemporal Features with 3D Convolutional Networks. 2015; <http://arxiv.org/abs/1412.0767>, arXiv:1412.0767 [cs].
- (44) Arnab, A.; Dehghani, M.; Heigold, G.; Sun, C.; Lučić, M.; Schmid, C. ViViT: A Video Vision Transformer. 2021; <http://arxiv.org/abs/2103.15691>, arXiv:2103.15691 [cs].
- (45) Ranftl, R.; Bochkovskiy, A.; Koltun, V. Vision Transformers for Dense Prediction. 2021; <http://arxiv.org/abs/2103.13413>, arXiv:2103.13413 [cs].
- (46) Damon, J.; Dietrich, S.; Vollert, F.; Gibmeier, J.; Schulze, V. Process dependent porosity and the influence of shot peening on porosity morphology regarding selective laser melted AlSi10Mg parts. *Additive Manufacturing* **2018**, *20*, 77–89.
- (47) Feng, S. C.; Lu, Y.; Jones, A. T.; Yang, Z. Additive Manufacturing In Situ and Ex Situ Geometric Data Registration. *Journal of Computing and Information Science in Engineering* **2022**, *22*.
- (48) Donegan, S. P.; Schwalbach, E. J.; Groeber, M. A. Multimodal Registration and Fusion of In Situ and Ex Situ Metal Additive Manufacturing Data. *JOM* **2021**, *73*, 3250–3262.
- (49) Arnhart, M.; Polonsky, A.; Ivanoff, T.; Mitchell, J.; Dagel, D.; Madison, J.; Jared, B. IN-SITU PYROMETRY AS AN INDICATOR FOR DEFECTS IN ADDITIVELY MANUFACTURED METALS - REVISITED. Proposed for presentation at the TMS in Anaheim, California. 2022.

- (50) Iebba, M.; Astarita, A.; Mistretta, D.; Colonna, I.; Liberini, M.; Scherillo, F.; Pirozzi, C.; Borrelli, R.; Franchitti, S.; Squillace, A. Influence of Powder Characteristics on Formation of Porosity in Additive Manufacturing of Ti-6Al-4V Components. *Journal of Materials Engineering and Performance* **2017**, *26*, 4138–4147.
- (51) Reutzell, E.; Petrich, J.; Corbin, D. J.; Snow, Z. Application of Machine Learning to Monitor Metal Powder-Bed Fusion Additive Manufacturing Processes. **2023**,
- (52) Shrestha, S.; Starr, T.; Chou, K. A Study of Keyhole Porosity in Selective Laser Melting: Single-Track Scanning With Micro-CT Analysis. *Journal of Manufacturing Science and Engineering* **2019**, *141*.
- (53) Cacace, S.; Semeraro, Q. On the Lack of fusion porosity in L-PBF processes. *Procedia CIRP* **2022**, *112*, 352–357.
- (54) Long, J.; Shelhamer, E.; Darrell, T. Fully Convolutional Networks for Semantic Segmentation. 2015; <http://arxiv.org/abs/1411.4038>, arXiv:1411.4038 [cs].
- (55) Jadhav, Y.; Berthel, J.; Hu, C.; Panat, R.; Beuth, J.; Barati Farimani, A. StressD: 2D Stress estimation using denoising diffusion model. *Computer Methods in Applied Mechanics and Engineering* **2023**, *416*, 116343.
- (56) Bahdanau, D.; Cho, K.; Bengio, Y. Neural Machine Translation by Jointly Learning to Align and Translate. 2016; <http://arxiv.org/abs/1409.0473>, arXiv:1409.0473 [cs, stat].
- (57) Vaswani, A.; Shazeer, N.; Parmar, N.; Uszkoreit, J.; Jones, L.; Gomez, A. N.; Kaiser, L.; Polosukhin, I. Attention Is All You Need. 2023; <http://arxiv.org/abs/1706.03762>, arXiv:1706.03762 [cs].
- (58) Li, Z.; Shu, D.; Barati Farimani, A. Scalable transformer for pde surrogate modeling. *Advances in Neural Information Processing Systems* **2024**, *36*.

- (59) Dosovitskiy, A.; Beyer, L.; Kolesnikov, A.; Weissenborn, D.; Zhai, X.; Unterthiner, T.; Dehghani, M.; Minderer, M.; Heigold, G.; Gelly, S.; Uszkoreit, J.; Houlsby, N. An Image is Worth 16x16 Words: Transformers for Image Recognition at Scale. 2021; <http://arxiv.org/abs/2010.11929>, arXiv:2010.11929 [cs].
- (60) Gotmare, A.; Keskar, N. S.; Xiong, C.; Socher, R. A Closer Look at Deep Learning Heuristics: Learning rate restarts, Warmup and Distillation. 2018; <http://arxiv.org/abs/1810.13243>, arXiv:1810.13243 [cs, stat].
- (61) Ikeuchi, K., Ed. *Computer Vision: A Reference Guide*; Springer International Publishing: Cham, 2021.
- (62) Dagel, D. J.; Grossetete, G. D.; MacCallum, D. O.; Korey, S. P. Four-color imaging pyrometer for mapping temperatures of laser-based metal processes. Baltimore, Maryland, United States, 2016; p 986103.